Article

Structure and Electrical Behavior of Hafnium-Praseodymium Oxide Thin Films Grown by Atomic Layer Deposition

Kaupo Kukli [1,*], Lauri Aarik [1], Guillermo Vinuesa [2], Salvador Dueñas [2], Helena Castán [2], Héctor García [2], Aarne Kasikov [1], Peeter Ritslaid [1], Helle-Mai Piirsoo [1] and Jaan Aarik [1]

[1] Institute of Physics, University of Tartu, W. Ostwaldi 1, 50411 Tartu, Estonia; lauri.aarik@ut.ee (L.A.); aarne.kasikov@ut.ee (A.K.); peeter.ritslaid@ut.ee (P.R.); helle-mai.piirsoo@ut.ee (H.-M.P.); jaan.aarik@ut.ee (J.A.)

[2] Department of Electronics, University of Valladolid, Paseo Belén 15, 47011 Valladolid, Spain; guillermo.vinuesa@alumnos.uva.es (G.V.); sduenas@ele.uva.es (S.D.); helcas@tel.uva.es (H.C.); hecgar@tel.uva.es (H.G.)

* Correspondence: kaupo.kukli@ut.ee

Abstract: Crystal structure and electrical properties of hafnium-praseodymium oxide thin films grown by atomic layer deposition on ruthenium substrate electrodes were characterized and compared with those of undoped HfO_2 films. The HfO_2 reference films crystallized in the stable monoclinic phase of HfO_2. Mixing HfO_2 and PrO_x resulted in the growth of nanocrystalline metastable tetragonal HfO_2. The highest relative permittivities reaching 37–40 were measured for the films with tetragonal structures that were grown using HfO_2:PrO_x cycle ratio of 5:1 and possessed Pr/(Pr + Hf) atomic ratios of 0.09–0.10. All the HfO_2:PrO_x films exhibited resistive switching behavior. Lower commutation voltages and current values, promising in terms of reduced power consumption, were achieved for the films grown with HfO_2:PrO_x cycle ratios of 3:1 and 2:1 and showing Pr/(Pr + Hf) atomic ratios of 0.16–0.23. Differently from the undoped HfO_2 films, the Pr-doped films showed low variability of resistance state currents and stable endurance behavior, extending over 10^4 switching cycles.

Keywords: hafnium oxide; praseodymium oxide; atomic layer deposition; crystal structure; dielectric properties; resistive switching

Citation: Kukli, K.; Aarik, L.; Vinuesa, G.; Dueñas, S.; Castán, H.; García, H.; Kasikov, A.; Ritslaid, P.; Piirsoo, H.-M.; Aarik, J. Structure and Electrical Behavior of Hafnium-Praseodymium Oxide Thin Films Grown by Atomic Layer Deposition. *Materials* **2022**, *15*, 877. https://doi.org/10.3390/ma15030877

Academic Editors: Lukasz Wachnicki and Sylwia Gierałtowska

Received: 19 December 2021
Accepted: 19 January 2022
Published: 24 January 2022

Publisher's Note: MDPI stays neutral with regard to jurisdictional claims in published maps and institutional affiliations.

Copyright: © 2022 by the authors. Licensee MDPI, Basel, Switzerland. This article is an open access article distributed under the terms and conditions of the Creative Commons Attribution (CC BY) license (https://creativecommons.org/licenses/by/4.0/).

1. Introduction

HfO_2, as a high-permittivity metal oxide, has attracted marked attention as a functional component of different nanoelectronic devices. HfO_2 films have been studied and exploited as gate dielectric layers in both planar [1] and three-dimensional (3D) Fin-type [2] field-effect transistors. In order to modify the phase composition and enhance the functionality of the films, HfO_2 has been doped with foreign metals or metal oxides. For example, Al-doped phase-stabilized HfO_2 has been investigated as a dielectric for volatile dynamic random access memories [3]. In addition, stabilization of orthorhombic phase of HfO_2 by doping with aluminum [4,5] or praseodymium [6] has been reported to cause the appearance of ferroelectric behavior, opening up routes to HfO_2-based nonvolatile memories.

Regarding other potential applications of HfO_2, resistive switching (RS) memory devices [7–17] are of significant importance. RS media based on metal oxides have been of interest for materials scientists and engineers over several decades, dating back to the beginning of 1960-ies [7]. The diversity in the choice of the materials suited to this application is still large, as one can decide on the basis of several recent reviews [7–10]. Amongst the metal oxide thin films under investigation, different compounds, such as TiO_2, Al_2O_3, Ta_2O_5, ZrO_2, or HfO_2, can be considered.

HfO_2 thin films have been examined as RS media in several studies [12–17]. At the same time, to improve the RS performance, the effect of doping has also been investigated.

For instance, aluminum has been used as a dopant in RS HfO_2 films [18,19]. In a long list of other dopants used in oxide films, praseodymium (Pr) is the one that has been applied to improve RS properties of CeO_2 [20] and ZnO [21]. Moreover, Pr has found application as a component of a rather complex compound, $Pr_{0.7}Ca_{0.3}MnO_3$, examined as RS media in a number of studies [22–27]. In the case of HfO_2, Pr has mainly attracted attention as a dopant allowing stabilization of metastable phases with ferroelectric properties and high permittivity values [6]. These results led us to a conclusion that the further investigation of Pr-doped HfO_2 as an electronic material could be of significant interest, especially because the Pr impurities might also influence the RS performance of HfO_2.

Among the methods that can be used for the deposition of HfO_2 thin films, atomic layer deposition (ALD) is the one that allows conformal coating of substrates with complex shapes [3]. For this reason, the method is of particular importance in the production of electronic devices with 3D integration [2,3]. The HfO_2 thin films have been grown by ALD from different hafnium precursors [4,5,13–15,18,19,28] of which $HfCl_4$ is a carbon-free metal precursor allowing self-limited ALD-type growth in an extremely wide temperature range extending from 225 to 940 °C [28]. H_2O has been the most common oxygen precursor applied in ALD of HfO_2. However, ozone (O_3) as a hydrogen-free oxygen precursor has also been exploited for ALD together with $HfCl_4$ [29–32]. As $HfCl_4$ and O_3 had advantages in the deposition of films with low contamination levels, the ALD process based on these precursors was also employed in the present work.

Praseodymium oxide (PrO_x) thin films have been grown using chemical vapor deposition [33] as well as ALD [34] routes based on $Pr(thd)_3$ (thd = 2,2,6,6-tetramethyl-3,5-heptanedione). The paper by Hansen et al. [34] implies that H_2O does not serve as an appropriate co-reactant together with $Pr(thd)_3$ because this precursor combination does not yield films with well-developed crystallinity and sufficient thickness uniformity. Another study on crystallization in lanthanide oxides [35] has indicated that PrO_x films can be grown at 300 °C from $Pr(thd)_3$ and O_3. However, the films tend to be of multiphase composition, containing Pr_6O_{11} and cubic PrO_2 phases due to the ability of this lanthanide to form Pr^{3+} and Pr^{4+} oxides and the latter's mixed phases.

Mixed PrO_x and hafnium oxide films have been grown by ALD using $Pr(thd)_3$, $HfCl_4$, and O_3 as the precursors [36]. In these experiments, the effects of deposition process parameters on the growth rate, crystal structure, phase composition, and optical properties (refractive index, optical bandgap, and photoluminescence efficiency) of the films were characterized [36]. The results revealed that the main phases observed in the praseodymium oxide films were PrO_2 formed at 225–250 °C, Pr_6O_{11} formed at 275 °C, and Pr_7O_{12} and Pr_6O_{11} formed at 300–325 °C. The studies on ALD of HfO_2 from $HfCl_4$ and O_3 [32] have revealed that the monoclinic phase is predominantly obtained in the thicker (>40 nm) films at the substrate temperatures ranging from 225 to 600 °C. However, in the thinner films, the metastable cubic, tetragonal, or orthorhombic phase has also been observed [32]. Pr-doping stimulated the growth of the metastable phases while at sufficiently high Pr concentrations; only the tetragonal t'-form has been obtained in the films [36].

In nanoelectronics, ruthenium (Ru), as a noble metal with a high work function, has been of interest and studied as an electrode material of dynamic random access memory capacitors [37–40] with high permittivity dielectrics and very high capacitance density values [37]. Ru has also been applied as an electrode material of RS stacks [41–43]. Ru electrodes of RRAM devices have been directly contacted to Nb_2O_5 [44], tantalum oxide [43,45], or HfO_2 films [41]. Depending on the processes investigated, the Ru electrodes [43] and/or switching metal oxide layers [42,46] may have been grown by ALD.

Although RS can be based on several underlying mechanisms, the switching phenomena in the metal–insulator–metal stacks with metal oxide dielectrics and electrochemically inactive metal electrodes are usually governed by the valence change mechanism (VCM) [46,47]. In this type of RS media, conductive filaments are formed by oxygen vacancies and grow in the dielectric until they connect metal electrodes. To create these filaments for the first time, it is usually necessary to perform an electroforming process applying

voltage values that are higher than those needed later for RS [48,49]. Thereafter, using voltage with inverted polarity, the filament can be partially disrupted (RESET event). To form the conductive filament again (SET event), a voltage with the same polarity as in the electroforming process, but with a much lower value, can be applied [50]. VCM has been suggested to be the main RS mechanism in the structures with HfO_2 dielectric and with inert metal electrodes [51,52]. Recently, the conductive filamentary model has been described in an RS medium consisting of alloyed $HfTiO_x$ films in silicon-based contact hole structures where the oxide was grown by ALD from tetrakisethylmethyl(amino) hafnium, titanium tetraisopropoxide, and water [53]. The VCM of RS has also been observed in the case of other oxides. For instance, there is experimental evidence of this filamentary conduction in Ta_2O_5-based films [54]. Therefore, the same RS mechanism was expected to appear in Pr-doped HfO_2 as well.

The present work was performed to investigate the effect of Pr-doping on the electrical properties of HfO_2, in particular, on the permittivity and RS performance. High permittivity together with high bandgap values is important in applications where HfO_2 is used as a high-permittivity gate or capacitor dielectric. Earlier studies have revealed that Pr doping of HfO_2 causes an increase in the bandgap values and stabilization of a metastable tetragonal phase [36] that was expected to lead to the permittivity increase. A goal of this work was to obtain experimental data on the permittivity of Pr-stabilized metastable HfO_2. Another goal of this work was to investigate if the stabilization of the metastable phase and increase in the bandgap energy influence the RS performance, particularly the low to high resistance state ratio during RS and the stability of that ratio in terms of the endurance of such samples on ruthenium electrodes.

2. Materials and Methods

The Pr-doped HfO_2 films studied in this work were deposited in an in-house built hot-wall flow-type ALD reactor [55] at 325 °C using $HfCl_4$ (99.9 %, Aldrich Chemicals Co. St. Louis, MO, USA) and O_3 as the precursors for deposition of HfO_2 [32], and $Pr(thd)_3$ (Volatec Oy, Porvoo, Finland) and O_3 for adding PrO_x to the film material [36]. Nitrogen (99.999%, AS Linde Gas, Tallinn, Estonia) was the carrier as well as purging gas in these experiments. The deposition process parameters were similar to those used earlier [36]. During the deposition, the net gas pressure in the reactor was kept at 200–220 Pa. O_3 was produced from O_2 (99.999% purity, AS Linde Gas, Tallinn, Estonia) using a BMT 802N ozone generator (BMT Messtechnik, Stahnsdorf, Germany). The O_3 concentration, measured by a BMT 964 ozone analyzer (BMT Messtechnik, Stahnsdorf, Germany) in the O_3/O_2 mixture at the outlet of the O_3 generator, was 240–260 g/m^3. The partial pressure of the O_3/O_2 mixture was set at 22 Pa in the reaction chamber during the oxygen precursor pulses.

The Ru bottom electrodes were deposited on Si(100) substrates at room temperature by DC-magnetron sputtering in Ar (99.999%) environment using a Ru (99.95%) planar target of 25 mm in diameter. The pressure during the sputtering process was 3×10^{-3} mbar, the DC-power was 2 W and the distance between target and substrate was 60 mm.

For the deposition of Pr-doped HfO_2, supercycles—including one cycle of $Pr(thd)_3$-O_3 per 2–5 cycles of $HfCl_4$-O_3—were repeated 25–50 times to obtain 19–50-nanometer thick Pr-doped films studied in this work. Each ALD cycle used for deposition of HfO_2 included a $HfCl_4$ pulse, purge, O_3 pulse, and another purge with durations of 5, 2, 5, and 5 s, respectively, while those used for deposition of PrO_x included a $Pr(thd)_3$ pulse, purge, O_3 pulse, and purge with durations of 5, 2, 5, and 5 s, respectively. No post-deposition annealing was applied for samples studied in this work.

The crystalline phases formed in the films were determined by the grazing incidence XRD (GIXRD) method using an X-ray diffractometer SmartLab (Rigaku, Tokyo, Japan) and Cu Kα radiation. The incidence angle chosen for the GIXRD measurements was 0.42°, corresponding to the scattering depth of 20 nm in cubic PrO_2 and 11 nm in monoclinic HfO_2 [36]. The diffractometer was also employed for X-ray reflection (XRR) measurements to determine the film thickness and surface roughness values. Additionally, the film thick-

nesses were measured with a GES5E spectroscopic ellipsometer (Semilab Sopra, Budapest, Hungary). Combining these two methods, the thicknesses of thinner (19–28 nm) films were determined with an accuracy better than ±2 nm while those of thicker (50–65 nm) films were obtained with an accuracy of ±3 nm. The mass thicknesses and elemental compositions of the films were determined with X-ray fluorescence (XRF) analyzer ZSX400 (Rigaku, Tokyo, Japan). Scanning electron microscope (SEM) Helios NanoLab 600 (FEI Company, Hillsboro, OR, USA) was used in a high-resolution mode (at an acceleration voltage of 10 kV and electron beam current of 86 pA) to characterize the surface microstructure.

For the electrical measurements, titanium top electrodes with circular geometry and thicknesses of 50 nm were electron-beam evaporated on the dielectric through a shadow mask at 230 °C. The Ti electrodes used in the measurements had areas of 0.002 and 0.052 mm^2. Electrical measurements were carried out in a probe station using a Keithley 4200-SCS semiconductor analyzer (Keysight Technologies, Cleveland, OH, USA). In the DC measurements, the bias voltage was applied to the top electrode while the bottom electrode remained grounded. To initiate RS, every sample required an electroforming procedure that was carried out as a voltage sweep with positive bias using a current compliance set at 1 µA to avoid irreversible breakdown of devices. In general, the electroforming took place between 7 and 13 V. The current–voltage (I-V) curves were obtained by applying positive and negative voltage sweeps to switch between the resistance states (bipolar RS), while the memory maps [56,57] were measured by reading the current value at 0.1 V after applying every increasing (or decreasing) voltage value used in the I-V envelope curves. To carry out the endurance measurements, a high number of relatively fast RS cycles were recorded. Each cycle was defined by a voltage pulse sequence of V_{set}, 0.1 V, $-V_{reset}$, and 0.1 V with switching pulse time durations of 0.1 s for V_{set} as well as for V_{reset}. Capacitance frequency measurements were carried out by applying a 30-millivolt signal without a DC bias in the 10 kHz–1 MHz frequency range.

3. Results and Discussion

3.1. Composition and Structure

The Pr/(Hf + Pr) atomic ratio in the HfO_2:PrO_x films was appreciably correlated with the ratio of HfO_2 and Pr_2O_3 deposition cycles (Figure 1) and equaled to 0.23, 0.16, and 0.10 in the 28-, 23-, and 19-nanometer thick films, grown using the HfO_2:PrO_x cycle ratios of 2:1, 3:1, and 5:1, respectively. In the 50-nanometer thick film grown using the HfO_2:PrO_x cycle ratio of 5:1, the Pr/(Hf + Pr) atomic ratio was 0.09.

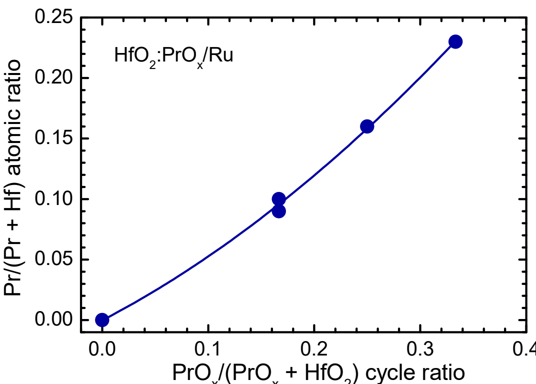

Figure 1. Pr/(Hf + Pr) atomic ratio as a function of PrO_x/(HfO_2 + PrO_x) cycle ratio, used for ALD of HfO_2:PrO_x films.

As expected, the Pr content influenced the crystal structure of the HfO_2:PrO_x films. As can be seen in Figure 2, the 65-nanometer thick HfO_2 reference film, i.e., the one which did not contain PrO_x, was unambiguously crystallized in the form of the stable monoclinic polymorph. Furthermore, the expected and also obvious effect of the doping

was the stabilization of a metastable polymorph. It should be mentioned, however, that the distinction between metastable cubic, tetragonal, and even orthorhombic phases of HfO_2 was quite complicated, considering the small crystallite sizes accompanied by peak broadening and possible effects of doping and substrate structure, causing shifts in the peak positions. The corresponding reflections, peaking at 30.3, 35.5, 50.3, 60.5, and 63.0 degrees (Figure 2), were attributable to the 101, 110, 112, 211, and 202 reflections of tetragonal HfO_2 (PDF card 01-078-5756). At the same time, the reflections might also be assigned as 111, 002, 022, 113, and 222 reflections of the cubic HfO_2 (PDF card 96-900-9017), or as 111, 020, 022, 113, and 311 reflections of the orthorhombic HfO_2 (PDF card 00-021-0904). However, it is worth mentioning that the refinement of similar diffraction patterns of Pr-doped HfO_2 thin films grown by ALD on silicon substrates to thicknesses of 140–328 nm revealed the formation of tetragonal t' form rather than other phases of HfO_2 in the films with Pr/(Pr + Hf) atomic ratios $\geq$ 0.095 [36]. The tetragonal t' form [58] is characterized by the relatively small tetragonality of its lattice (with lattice parameter ratios c/a ranging from 1.004 to 1.012 for the pseudo-fluorite unit cell), and therefore is an intermediate structure form between the cubic and tetragonal HfO_2. Nevertheless, it is also possible that the structure of the relatively thin films deposited on Ru in the present work had not been fully formed and, for this reason, was of a multiphase nature. In particular, low GIXRD reflection intensities of the thinner films grown with a HfO_2:PrO_x cycle ratio of 5:1 indicated the presence of amorphous and/or nanocrystalline phases with poorly developed structure in the films.

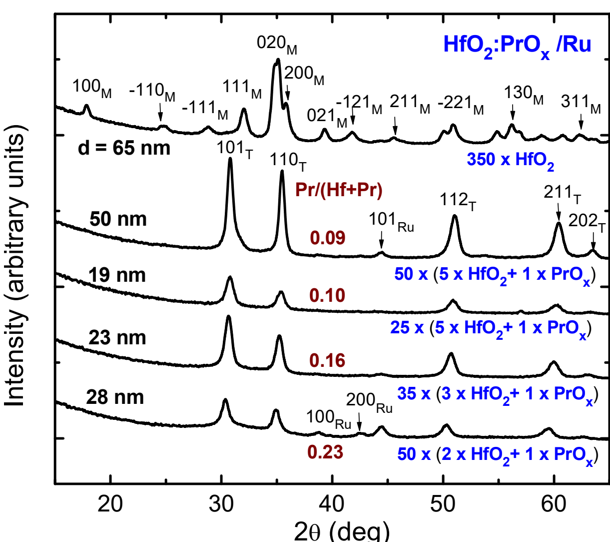

Figure 2. Grazing incidence diffraction patterns from HfO_2:PrO_x films deposited on Ru. The growth cycle sequences for HfO_2 and PrO_x, and Miller indexes attributed to either tetragonal (T) or monoclinic (M) phases of HfO_2 are shown at the diffraction patterns. Reflections from substrate Ru layers are denoted by corresponding labels. The film thicknesses (d) and compositions (Pr/(Hf + Pr) atomic ratios) are also indicated by labels.

Although no direct correlation between the resistance state values and dielectric thickness had been observed in the VCM type RS media, based on HfO_2 [59] and other media [60], the dependence of the permittivity and RS performance on the structure development related to the dielectric thickness (Figure 2) could not be neglected. However, the results of electrical measurements presented below were dominantly influenced by the chemical and phase composition rather than by the thickness of the dielectric. For this reason, the further downscaling of the thickness was not studied in the present work.

The fitting of XRR data, measured for a 19.5-nanometer-thick Ru film used as a bottom electrode (Figure 3a), yielded a surface roughness value as low as 0.4 $\pm$ 0.2 nm. Thereby, the density of Ru was found to be 12.5 g/cm^3, that is, close to the bulk value. The SEM

studies confirmed the almost featureless and artifact-free nature of Ru electrode films (Figure 3b), allowing one to rely on smooth contact interfaces between the electrode and the RS medium. This was an important result because the SET events of the RS processes took place at positive voltages applied to the top electrodes. In such a case, the smoothness of the bottom electrode was assumed to reduce the parasitic leakage currents related to the electronic conduction and allowed us to expect reliable and reproducible electrical performance, uniform and stable over the electrode matrix formed on a sample used for electrical studies.

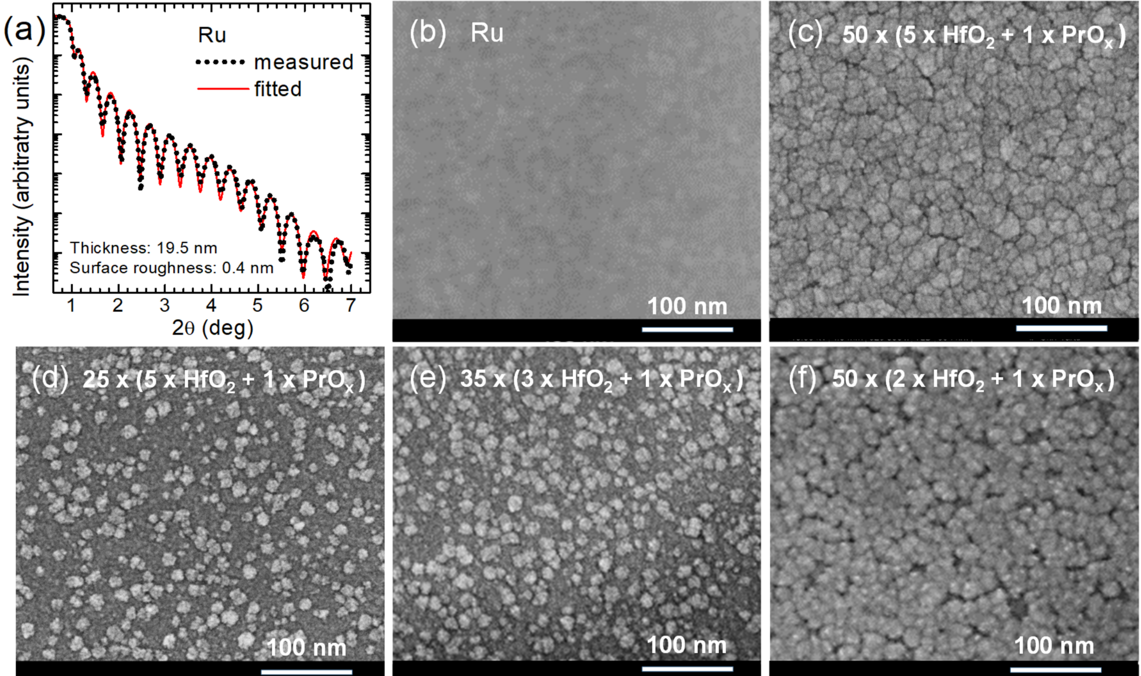

Figure 3. (**a**) XRR pattern on bare Ru bottom electrode, and (**b**–**f**) SEM images of (**b**) bare Ru bottom electrode, and (**c**–**f**) surfaces of HfO_2:PrO_x films deposited using cycle sequences indicated by labels.

The thicker dielectric film grown using HfO_2:PrO_x cycle ratio of 5:1 evidently consisted of densely packed grains (Figure 3c). A surface roughness of 1.9 nm, obtained from XRR measurements of this film, was notably higher than that of the Ru surface. For comparison, the surface roughness of a HfO_2 film of similar thickness was 1.7 nm. Smaller but distinctive grain-like features were observed by SEM on the surfaces of 2–3 times thinner oxide films (Figure 3d–f). The surface roughness values of these films grown using the HfO_2:PrO_x cycle ratios of 5:1, 3:1, and 2:1 were 0.6, 1.4, and 1.2 nm, respectively. It is worth noting that the SEM images as well as surface roughness values were consistent with the degrees of crystallization characterized by GIXRD (Figure 2).

3.2. Dielectric Properties

Figure 4 depicts the results of capacitance frequency measurements carried out on HfO_2:PrO_x films deposited on common Ru bottom electrodes and supplied with top electrodes arranged in a matrix. The capacitance did not show marked dispersion in a frequency range of 10–1000 kHz (Figure 4). This result could be considered as a plausible indication of the insignificant role of the relatively free space charge. Expectedly and most clearly, the capacitance correlated to the film thickness. However, the relative permittivity that depended on the phase composition of the HfO_2:PrO_x films (Figure 2) also influenced the capacitance values.

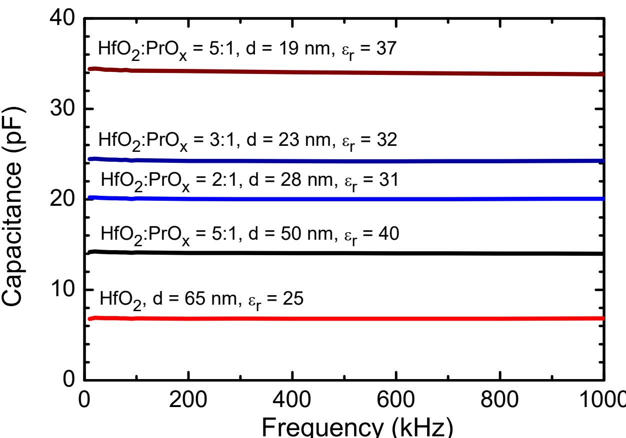

Figure 4. Capacitance dispersion curves measured from $HfO_2:PrO_x$ films deposited. $HfO_2:PrO_x$ cycle ratios and film thicknesses are indicated by labels. Indicated are also the average relative permittivity values calculated at 100 kHz using the common parallel plate capacitor stack formula. The area of the capacitor electrodes used was 0.052 mm^2. The uncertainty of the measurements did not exceed 10%.

The relative permittivity values were calculated from the mean capacitance values measured at 100 kHz. The highest permittivities, 37 and 40, were achieved from the calculations for the films deposited using a $HfO_2:PrO_x$ cycle ratio of 5:1 to the thicknesses of 19 and 50 nm, respectively. The GIXRD data (Figure 2) and results of the more complex analysis performed earlier [36] indicated that both films contained tetragonal phase (t' form), with the most intense reflections of 101 and 110, apparent in their diffraction patterns. The 23 and 28 nm thick films that were grown using $HfO_2:PrO_x$ cycle ratios of 3:1 and 2:1, and crystallized in the same metastable polymorph, possessed relative permittivities of 32 and 31, respectively. The lowest permittivity value that was equal to 25 was measured for the undoped HfO_2 film, which was grown to the thickness of 65 nm, and contained monoclinic HfO_2 (Figure 2).

Regarding the literature data, Zhao and Vanderbilt [61] obtained in their first-principles calculations that orientationally averaged static dielectric constants should be 29, 70, and 16 for the cubic, tetragonal, and monoclinic HfO_2 phases, respectively. In this connection, the permittivity values measured in the present study might have been related to the polymorphic composition of the films under discussion (Figure 2). The permittivity values extending to 40 (Figure 4) could thus be due to the presence of the tetragonal HfO_2 phase in the films. In this case, the value of the relative permittivity, although lower than that predicted by the first-principles calculations, could herewith be reasoned by the reduced tetragonality of the t' form or possible co-existence of tetragonal, cubic, and amorphous phases in the corresponding films. In contrast, the relative permittivity value as high as 25 (Figure 4), measured for the undoped HfO_2 film was higher than that attributed to the monoclinic HfO_2 [61]. This might, supposedly, become explained by a minor contribution of metastable phases that could also be present in the films.

In earlier studies of Pr-doped HfO_2 thin films that were grown by chemical solution deposition method and annealed at 800 °C, relative permittivity values of 23.5, 29.7, and 32.1 were obtained at Pr concentrations of 5, 10, and 15 mol%, respectively, while the corresponding value for an undoped HfO_2 film was determined to be 18.3 [6]. The crystalline phases observed were the monoclinic one in the undoped films, the orthorhombic phase in the films with 5 mol% Pr, and the cubic phase in the films with 10 and 15 mol% Pr [6]. Comparing these results with those of theoretical calculations [61] and with the permittivity values obtained for ALD films in our work (Figure 4), one can conclude that the formation of the tetragonal structure was the main reason for the high permittivity values of our films deposited using a $HfO_2:PrO_x$ cycle ratio of 5:1.

The decrease in the permittivity observed with the decrease of the HfO_2:PrO_x cycle ratio to 2:1 and increase of the Pr/(Pr + Hf) atomic ratio from 0.10 to 0.23 was probably caused by a decreasing amount of tetragonal phase in the films and/or decrease in the tetragonality of the t' form of HfO_2 with increasing concentration of Pr. The decrease in the tetragonality of the t' form with increasing concentrations of rare-earth dopant in HfO_2, has been observed, for instance, in the case of yttria-doped HfO_2 [60]. Unfortunately, because of relatively wide reflections in the GIXRD patterns of our films (Figure 2), revealing this kind of change in the crystal structure was not possible in the present work.

Another effect that might have contributed to the permittivity decrease observed with the increase of the Pr/(Pr + Hf) atomic ratio from 0.10 to 0.23 was the doping anisotropy that was most significant in the films grown with a HfO_2:PrO_x cycle ratio of 5:1. In the growth direction of these films, the Pr concentration varied with a period of 0.8–1.0 nm, approximately. This value was evidently larger than the in-plane distance between Pr^{3+} or Pr^{4+} ions, provided that the solid-phase diffusion did not lead to uniform distribution of Pr in the films. For comparison, the Pr concentration was expected to vary with a period of 0.5–0.6 nm in the growth direction of the films deposited using a HfO_2:PrO_x cycle ratio of 2:1. In this case, the period of dopant concentration variation was closer to the in-plane distances between Pr^{3+} or Pr^{4+} ions and, for this reason, the Pr distribution was more uniform than that in the films deposited with a HfO_2:PrO_x cycle ratio of 5:1.

Finally, the lower permittivity of PrO_x compared to that of tetragonal HfO_2 could be a reason for the permittivity decrease observed for Pr-doped HfO_2 with the decrease of the HfO_2:PrO_x cycle ratio from 5:1 to 2:1. According to the literature data, the relative permittivity values of polycrystalline PrO_x films have ranged from 8 to 26 [62,63] being higher for Pr_2O_3 and lower for PrO_2-rich films [62]. Therefore, to obtain the highest permittivity values, the Pr concentration in the Pr-doped HfO_2 films should not exceed significantly the value corresponding to the transition from the monoclinic to the tetragonal phase.

The conductivity of metal oxide dielectrics is directly related to their bandgap widths. On the other hand, doping with foreign elements—otherwise beneficial in terms of the stabilization of high-permittivity phases—might introduce parasitic states in the bandgap which could, presumably, increase the conduction currents. For instance, in the case of doping HfO_2 with praseodymium (oxide), Pr^{3+} ions have energy levels in the bandgap of HfO_2 [64]. At the same time, however, the optical bandgap increased from 5.55–5.65 eV, determined for undoped HfO_2, to 5.72–5.78 eV in the doped films, where Pr/(Pr + Hf) = 0.15–0.20 and a tetragonal phase was formed [36]. Notably, also the theoretical calculations have predicted a wider bandgap for the metastable tetragonal/cubic HfO_2, compared to that of stable monoclinic HfO_2 [65]. Therefore the bandgap widening compensates, at least to some extent, for the contribution of the additional states generated in the bandgap by doping, thereby enabling the formation of HfO_2:PrO_x films appreciably insulating in the capacitor structures and in the low resistance state of RS devices.

3.3. Resistive Switching

The HfO_2 and HfO_2:PrO_x films, which were deposited in this work on Ru electrodes and supplied with Ti top electrodes, demonstrated RS behavior, expressed by clear current–voltage envelope curves characteristic of RRAM devices (Figure 5). The electroforming voltages did not vary systematically with the HfO_2:PrO_x ratio. All the samples demonstrated, however, an abrupt forming transitions at 11–13 V to a current value of 1 μA set as a compliance limit in order to prevent irreversible breakdown.

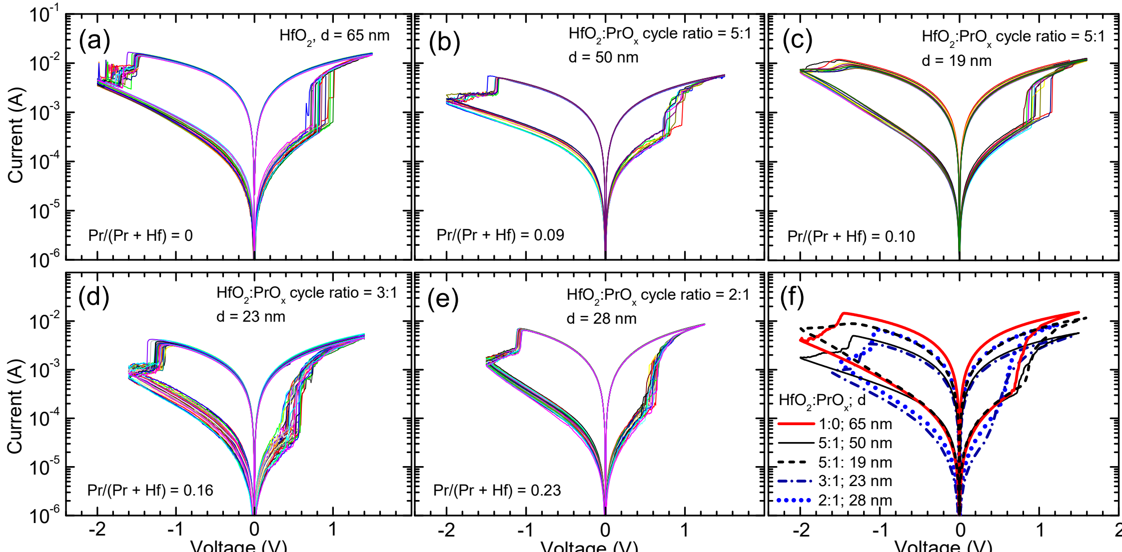

Figure 5. Current voltage envelope curves describing resistive switching of HfO_2:PrO_x films as-deposited on Ru electrode substrates. HfO_2:PrO_x deposition cycle ratios, Pr/(Pr + Hf) atomic ratios, and film thicknesses are indicated by labels in panels (**a**–**e**), where multiple (6–20) current–voltage curves are presented for the same film and device, measured consecutively and presented in different colors to enable better distinction. In panel (**f**), the averaged current–voltage curves are depicted comparatively.

The nature of the switching process (Figure 5) was bipolar, meaning that in the SET process, the conductive filaments were formed applying positive voltage in relation to the Ru electrode, while in the RESET process, the conductive paths were disrupted by applying voltage of the opposite polarity. The smallest electrodes with the average area of 0.002 mm^2 provided the most reliable results, that is, the initial electroforming process did not typically cause the dielectric breakdown, which otherwise would indicate issues with lateral homogeneity in the switching media.

The results depicted in Figures 5 and 6 demonstrate that the Pr concentration in the RS layer influenced the commutation voltages, current values in the low-resistive state (I_{LR}) and high-resistive state (I_{HR}) as well as the I_{LR}/I_{HR} ratio. The increase in the Pr/(Pr + Hf) atomic ratio from 0 to 0.10 caused a decrease in I_{LR} (Figures 5a–c and 6) and a minor increase in the set voltages (Figure 5a–c). At the same time, no considerable changes in I_{HR} appeared (Figure 6). As a result, the I_{LR}/I_{HR} ratios of the films that were grown using a HfO_2:PrO_x cycle ratio of 5:1 were lower than that of un-doped HfO_2.

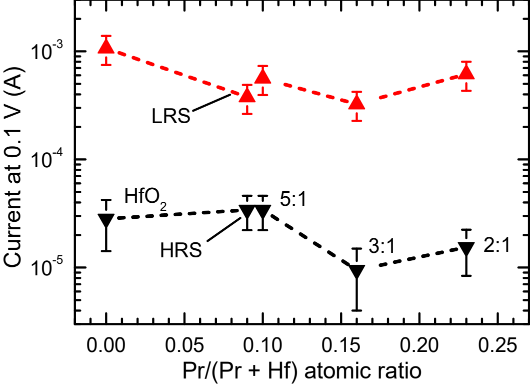

Figure 6. Current values recorded in low resistance state (LRS) and high resistance state (HRS) at a voltage value of 0.1 V (see Figure 5). The HfO_2:PrO_x ALD cycle ratios are indicated by labels at corresponding data points.

Comparison of the data for films with similar Pr/(Pr + Hf) atomic ratios (0.09 and 0.10) and very different thicknesses (50 and 19 nm, respectively) revealed minor differences in I_{LR} (Figure 5b,c and Figure 6). However, as can be seen in Figure 6, these differences were comparable to the experimental uncertainty related mainly to the deviation of results in successive measurements of the current-voltage (I-V) curves.

With the increase of the Pr/(Pr + Hf) atomic ratio to 0.16, obtained at a HfO_2:PrO_x cycle ratio of 3:1, the set and reset voltages and I_{HR} decreased while I_{LR}/I_{HR} increased to a level exceeding that of undoped HfO_2 (Figures 5d and 6). The further increase of the Pr/(Pr + Hf) atomic ratio to 0.23, observed in the films grown with a HfO_2:PrO_x cycle ratio of 2:1, did not influence the commutation voltages and I_{LR}/I_{HR} significantly (Figure 5d–f). However, I_{LR} and I_{HR} somewhat increased when compared to the corresponding values of the film grown using a HfO_2:PrO_x cycle ratio of 3:1 (Figure 6).

Besides the envelope I-V curves describing current values measured at the variable bias voltage values (Figure 5), memory maps were recorded at a constant reading voltage as well (Figure 7). In the latter case, the conduction currents were read at a voltage of 0.1 V in between the sequential programming voltage pulses. Two clearly defined plateaus were reached between sequential SET and RESET events (Figure 7). I-V loops, which can be termed as memory maps, were thus formed with prominently expressed memory windows between the high and low current states during multiple voltage loops (Figure 7).

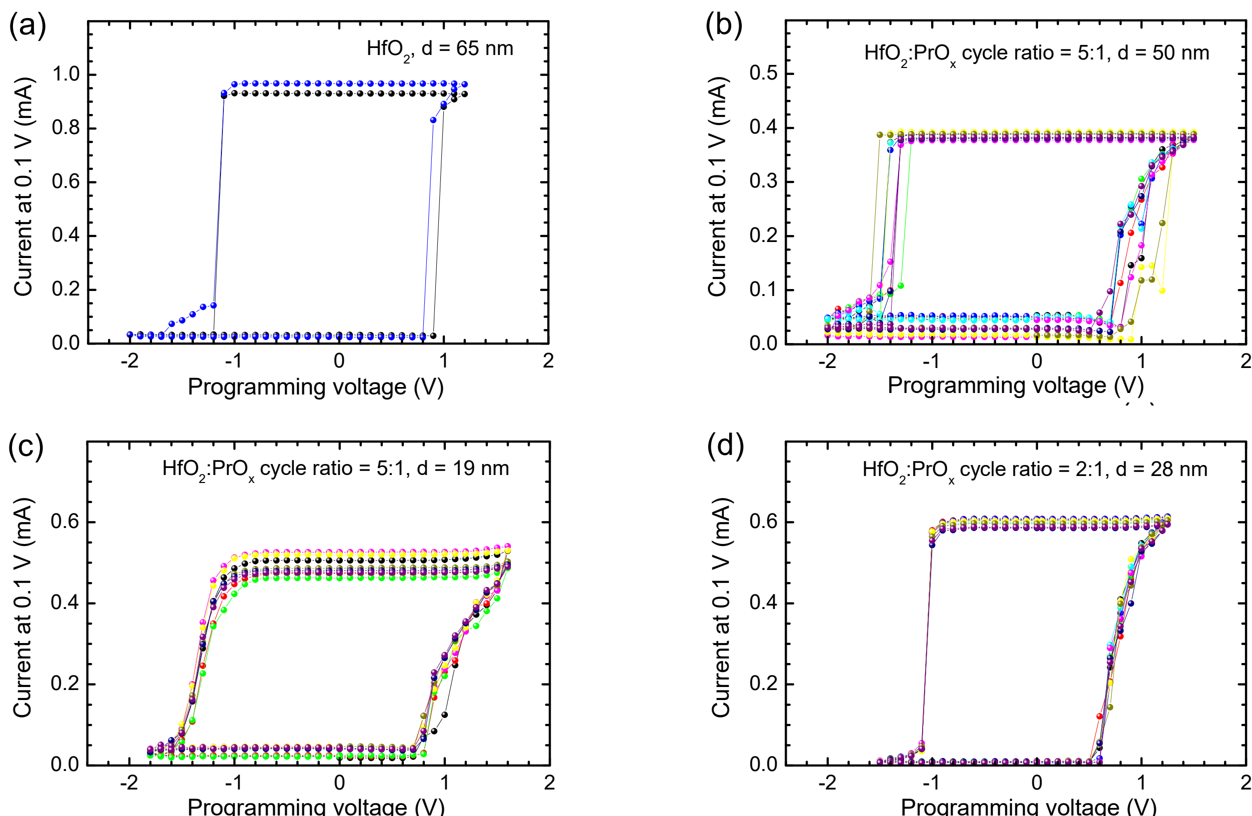

Figure 7. Current recorded at 0.1 V as a function of programming voltage used for biasing of the (**a**) HfO_2 and (**b**–**d**) HfO_2:PrO_x media before the current measurement. The HfO_2:PrO_x cycle ratios used for growing the films and film thicknesses are indicated by labels. Different colors correspond to different memory maps recorded for the same film and device. The Pr/(Pr + Hf) atomic ratios were (**b**) 0.09, (**c**) 0.10, and (**d**) 0.23.

The memory maps supported the results depicted in Figures 5 and 6, showing that narrower windows between the low and high resistivity states, that is lower I_{LR}/I_{HR} ratios, were obtained for the reference HfO_2 films ($I_{LR}/I_{HR} \approx 30$, Figure 7a) and especially for

the films deposited using HfO_2:PrO_x cycle ratio of 5:1 ($I_{LR}/I_{HR} \approx 10$, Figure 7b,c). The window between the low and high resistivity states was much wider in the case of samples containing oxide media grown with HfO_2:PrO_x cycle ratios of 3:1 (not shown) and 2:1 ($I_{LR}/I_{HR} \approx 60$, Figure 7d). Hence, rather than being a monotonic function of the Pr-content, the I_{LR}/I_{HR} ratio possessed a minimum value at Pr/(Pr + Hf) atomic ratios of 0.09–0.10, that is, at the HfO_2:PrO_x cycle ratio of 5:1. Earlier a significant dependence of RS performance on the doping level has been reported for Pr-doped ZnO films where the best functional ratio between resistance states appeared in the case of a certain stoichiometry [66]. The argument of an optimal composition has also been supported by the first-principles calculations made on HfO_x-based films [67]. Furthermore, thicknesses may also become more optimized at certain film stoichiometries [68], and would, consequently, require further more detailed parametrization.

Comparing the results depicted in Figures 5–7 with the GIXRD patterns (Figure 2), one can see that the I_{LR} decrease, caused by the increase of Pr/(Pr + Hf) to 0.09–0.10, was evidently related to the formation of the metastable phase in the films. The wider bandgap of this phase [36] and possible compensation of oxygen vacancies because of Pr-doping are the plausible reasons for this I_{LR} decrease. A probable reason for why the I_{HR} value did not decrease and, correspondingly, the I_{LR}/I_{HR} value decreased was the presence of some inclusions of monoclinic phase in the films deposited using a HfO_2:PrO_x cycle ratio of 5:1. An evidence of the monoclinic phase is a tail on the right side of the 30.3° reflection in the diffraction pattern of the 50-nm thick films grown with this cycle ratio (Figure 2). This tail was evidently related to the contribution of the 111 reflection of the monoclinic phase. Although the small amounts of the monoclinic phase were not able to have a marked effect on the low-resistive state, the contribution of those to the much lower I_{HR} values was still an expected result. Correspondingly, the absence of the monoclinic phase in the films grown with HfO_2:PrO_x cycle ratios of 3:1 and 2:1 and the formation of a more homogeneous crystalline phase in these films were reasons for lower I_{HR} and higher I_{LR}/I_{HR} values obtained. The latter films also possessed somewhat lower commutation voltages (Figures 5f and 7) than the rest of the samples did. This observation implies that the media which contain higher amounts of praseodymium and only metastable nanocrystalline phases might become better suited to low-power applications. Higher mobility of oxygen ions in these films might be one possible reason for lower commutation voltages observed.

Endurance measurements were carried out for samples with different doping levels to determine their reliability and resistance state variability during fast writing, erasing, and reading operations. In these measurements, a current compliance of 5 mA was set in order to prevent the irreversibly breaking of dielectrics when applying the commutation voltages in a short period of time. The use of compliance has been shown to improve the endurance characteristics in HfO_x-based RRAM [69]. However, the same functional windows between the high and low resistance states were not expected when comparing the results of endurance studies with the current-voltage envelope curves or memory maps.

First of all, the endurance characteristics presented in Figure 8 revealed higher stability of Pr-doped HfO_2 media compared to that of undoped HfO_2. In the case of samples with undoped HfO_2, the first instabilities in I_{LR} as well as I_{HR} appeared after applying a few hundred cycles, while a marked increase in I_{HR} was observed after 3000 cycles. In contrast, the RS layer grown using a HfO_2:PrO_x cycle ratio of 2:1 showed very stable I_{LR} as well as I_{HR} values up to the end of the endurance measurements (Figure 8). Therefore, the Pr-doping of HfO_2 and/or formation of metastable (tetragonal) phase in the RS medium play a significant in producing memory cells with superior RS performance.

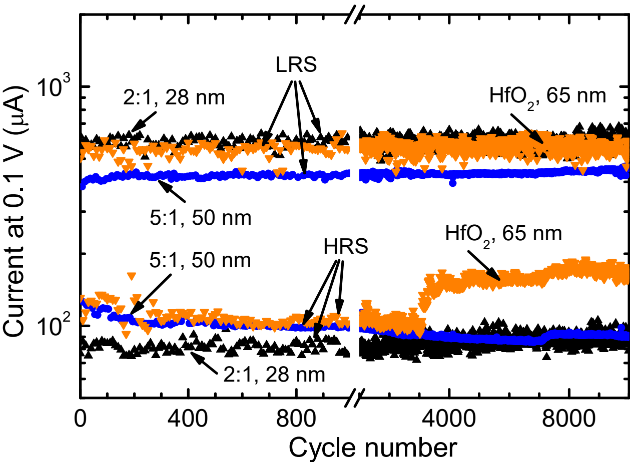

Figure 8. Endurance characteristics of HfO_2:PrO_x switching media measured in the small-signal regime. The HfO_2:PrO_x cycle ratios used for ALD of dielectrics and the dielectric layer thicknesses are indicated by labels at corresponding curves. I_{LR} and I_{HR} values for every tenth measurement cycle are depicted in the figure.

An even more interesting performance was observed in the case of samples with Pr-doped HfO_2 deposited using a HfO_2:PrO_x cycle ratio of 5:1 that yielded films with Pr/(Pr + Hf) atomic ratios of 0.09–0.10. Figure 8 demonstrates that with an increasing number of switching cycles, the I_{HR} value of a 50-nanometer thick film considerably decreased while the I_{LR} value increased resulting in a marked increase in the I_{LR}/I_{HR} ratio. It is noteworthy that a similar performance was observed for a 19-nanometer thick films with a Pr/(Pr + Hf) atomic ratio of 0.10. In both cases, the changes in I_{HR}, I_{LR}, and I_{LR}/I_{HR} were relatively smooth without significant random fluctuations of the current values. Therefore, it seems that the conductive filaments were additionally electroformed (stabilized) in this kind of RS medium during the endurance studies. Phase transitions leading to the formation of a more uniform crystal structure and/or more uniform distribution of Pr^{3+}/Pr^{4+} ions in the vicinity of switching filaments can be considered as the main mechanisms causing this kind of modification of the RS medium.

Comparison of our results with literature data confirmed the excellent performance of Pr-doped HfO_2 studied in this work compared to that of many other HfO_2-based undoped and doped RS media. Typical I_{LR}/I_{HR} values reported [16,70–75] have ranged from one to two orders of magnitude being well comparable to the corresponding values obtained in our work. However, I_{LR}/I_{HR} values as high as three orders of magnitude have also been reported for samples with optimized electrode structure [76]. In most cases, the endurance tests, if performed, have been limited to 1000 switching cycles [70,71,73,75] but reports about endurance tests up to 10^5 [72,74] and 10^8 [16] switching cycles have also been published. Comparing the results described in the latter papers with those obtained in our experiments one can still conclude that after optimization of the device processing procedures, Pr-doped HfO_2 can also become a promising candidate for application in resistive switching random access memories.

4. Conclusions

Our studies of Pr-doped HfO_2 thin films grown by ALD on ruthenium electrodes revealed superior properties of these films for different electronic applications. The films grown using HfO_2:PrO_x ALD cycle ratios, ranging from 5:1 to 2:1, crystallized in the tetragonal phase while the Pr/(Pr + Hf) atomic ratio ranged from 0.09 to 0.23 in these films. The relative permittivity values as high as 37–40 were measured for the films with Pr/(Pr + Hf) atomic ratios of 0.09–0.10. No considerable dependence of the permittivity on the measurement frequency was observed in a frequency range of 0.01–1 MHz. As the

films with this composition have also high bandgap values (5.72–5.78 eV), as revealed in our earlier work, they could successfully be applied as capacitor and gate dielectrics.

Additionally, stable-resistive switching performance was obtained in metal–dielectric–metal structures with HfO_2:PrO_x dielectrics, ruthenium bottom electrodes, and titanium top electrodes. In the structures with as-grown dielectrics, the I_{LR}/I_{HR} ratios ranged from 10 in the case of dielectrics with Pr/(Pr + Hf) atomic ratios of 0.09–0.10 to 60 in the case of dielectrics with Pr/(Pr + Hf) atomic ratios of 0.16–0.23. The resistive switching layers with Pr/(Pr + Hf) atomic ratios of 0.16–0.23 showed also lower I_{LR}, I_{HR}, and commutation voltage values compared to corresponding parameters recorded for devices with undoped HfO_2 dielectric. The endurance measurements demonstrated excellent stability of resistive switching in Pr-doped HfO_2 during 10^4 switching cycles. Thus, Pr-doped HfO_2 could be considered as a promising material for application in resistive switching memory devices as well.

Author Contributions: Conceptualization, K.K., L.A., S.D. and J.A.; methodology, G.V., L.A., J.A., H.G. and H.C.; investigation, G.V., L.A., A.K., P.R. and H.-M.P., resources, K.K., L.A. and H.C.; writing, K.K., G.V. and J.A.; funding acquisition, K.K., L.A., H.C. and S.D. All authors have read and agreed to the published version of the manuscript.

Funding: The work has partially been supported by Spanish Ministry of Science, Innovation and Universities grant TEC2017-84321-C4-2-R, with support of Feder funds; European Regional Development Fund project "Emerging orders in quantum and nanomaterials" (TK134); and Estonian Research Agency (projects PSG448 and PRG753).

Institutional Review Board Statement: Not applicable.

Informed Consent Statement: Not applicable.

Data Availability Statement: Not applicable.

Conflicts of Interest: The authors declare no conflict of interest.

References

1. Huff, H.R.; Hou, A.; Lim, C.; Kim, Y.; Barnett, J.; Bersuker, G.; Brown, G.A.; Young, C.D.; Zeitzoff, P.M.; Gutt, J.; et al. High-k gate stacks for planar, scaled CMOS integrated circuits. *Microelectron. Eng.* **2003**, *69*, 152–167. [CrossRef]
2. Tsormpatzoglou, A.; Tassis, D.H.; Dimitriadis, C.A.; Mouis, M.; Ghibaudo, G.; Collaert, N. Electrical characterization and design optimization of FinFETs with a TiN/HfO_2 gate stack. *Semicond. Sci. Technol.* **2009**, *24*, 125001. [CrossRef]
3. Kim, S.-G.; Hyun, C.-S.; Park, D.; Cho, T.-H.; Suk, J.-G.; Hong, H.-S.; Lee, K.-Y.; Oh, K.-S. Fully integrated 512 Mb DRAMs with HSG-merged-AHO cylinder capacitor. *Solid-State Electron.* **2006**, *50*, 1030–1034. [CrossRef]
4. Mueller, M.; Mueller, J.; Singh, A.; Riedel, S.; Sundqvist, J.; Schroeder, U.; Mikolajick, T. Incipient ferroelectricity in Al-doped HfO_2 thin films. *Adv. Funct. Mater.* **2012**, *22*, 2412–2417. [CrossRef]
5. Florent, K.; Lavizzari, S.; Popovici, M.; di Piazza, L.; Celano, U.; Groeseneken, G.; van Houdt, J. Understanding ferroelectric Al:HfO_2 thin films with Si-based electrodes for 3D applications. *J. Appl. Phys.* **2017**, *121*, 204103. [CrossRef]
6. Liu, H.; Zheng, S.; Chen, Q.; Zeng, B.; Jiang, J.; Peng, Q.; Liao, M.; Zhou, Y. Structural and ferroelectric properties of Pr doped HfO_2 thin films, fabricated by chemical solution method. *J. Mater. Sci. Mater. Electron.* **2019**, *30*, 5771–5779. [CrossRef]
7. Chen, E. ReRAM: History, Status, and Future. *IEEE Trans. Electron. Dev.* **2020**, *67*, 1420–1433. [CrossRef]
8. Carlos, E.; Branquinho, R.; Martins, R.; Kiazadeh, A.; Fortunato, E. Recent progress in solution-based metal oxide resistive switching devices. *Adv. Mater.* **2021**, *33*, 2004328. [CrossRef]
9. Gupta, V.; Kapur, S.; Saurabh, S.; Grover, A. Resistive random access memory: A review of device challenges. *IETE Tech. Rev.* **2020**, *37*, 377–390. [CrossRef]
10. Ader, C.; Falkenstein, A.; Martin, M. Transition between bipolar and abnormal bipolar resistive switching in amorphous oxides with a mobility edge. *Sci. Rep.* **2021**, *11*, 14384. [CrossRef]
11. Chakraborty, I.; Jaiswal, A.; Saha, A.K.; Gupta, S.K.; Roy, K. Pathways to efficient neuromorphic computing with non-volatile memory technologies. *Appl. Phys. Rev.* **2020**, *7*, 021308. [CrossRef]
12. Chen, W.; Lu, W.; Long, B.; Li, Y.; Gilmer, D.; Bersuker, G.; Bhunia, S.; Jha, R. Switching characteristics of W/Zr/HfO_2/TiN ReRAM devices for multi-level cell non-volatile memory applications. *Semicond. Sci. Technol.* **2015**, *30*, 075002. [CrossRef]
13. García, H.; Vinuesa, G.; Ossorio, Ó.G.; Sahelices, B.; Castán, H.; Dueñas, S.; González, M.B.; Campabadal, F. Study of the set and reset transitions in HfO_2-based ReRAM devices using a capacitor discharge. *Solid-State Electron.* **2021**, *183*, 108113. [CrossRef]
14. Ryu, J.-H.; Mahata, C.; Kim, S. Long-term and short-term plasticity of Ta_2O_5/HfO_2 memristor for hardware neuromorphic application. *J. Alloys Compd.* **2021**, *850*, 156675. [CrossRef]

15. Dueñas, S.; Castán, H.; García, H.; Miranda, E.; Gonzalez, M.B.; Campabadal, F. Study of the admittance hysteresis cycles in TiN/Ti/HfO_2/W-based RRAM devices. *Microelectron. Eng.* **2017**, *178*, 30–33. [CrossRef]
16. Rodriguez-Fernandez, A.; Cagli, C.; Perniola, L.; Miranda, E.; Suñé, J. Characterization of HfO_2-based devices with indication of second order memristor effects. *Microelectron. Eng.* **2018**, *195*, 101–106. [CrossRef]
17. Loy, D.J.J.; Dananjaya, P.A.; Chakrabarti, S.; Tan, K.H.; Chow, S.C.W.; Toh, E.H.; Lew, W.S. Oxygen vacancy density dependence with a hopping conduction mechanism in multilevel switching behavior of HfO_2-based resistive random access memory devices. *ACS Appl. Electron. Mater.* **2020**, *2*, 3160–3170. [CrossRef]
18. Wu, L.; Liu, H.; Li, J.; Wang, S.; Wang, X. A multi-level memristor based on Al-doped HfO_2 thin film. *Nanoscale Res. Lett.* **2019**, *14*, 177. [CrossRef]
19. Brivio, S.; Frascaroli, J.; Spiga, S. Role of Al doping in the filament disruption in HfO_2 resistance switches. *Nanotechnology* **2017**, *28*, 395202. [CrossRef]
20. Chen, N.; Li, S. Synthesis of oxygen-deficient and monodispersed Pr doped CeO_2 nanocubes with enhanced resistive switching properties. *IOP Conf. Ser. Mater. Sci. Eng.* **2019**, *576*, 012035. [CrossRef]
21. Kao, M.-C.; Chen, H.-Z.; Chen, K.-H.; Shi, J.-B.; Weng, J.-H.; Chen, K.-P. Resistive switching behavior and optical properties of transparent Pr-doped ZnO based resistive random access memory. *Thin Solid Films* **2020**, *697*, 137816. [CrossRef]
22. Seong, D.; Hassa, M.; Choi, H.; Lee, J.; Yoon, J.; Park, W.; Lee, M.; Oh, H.H. Resistive-switching characteristics of Al/$Pr_{0.7}Ca_{0.3}MnO_3$ for nonvolatile memory applications. *IEEE Electron. Dev. Lett.* **2009**, *30*, 919–921. [CrossRef]
23. Moon, K.; Park, S.; Lee, D.; Woo, J.; Cha, E.; Lee, S.; Hwang, H. Resistive-switching analogue memory device for neuromorphic application. In Proceedings of the 2014 Silicon Nanoelectronics Workshop (SNW), Honolulu, HI, USA, 8–9 June 2014; pp. 1–2. [CrossRef]
24. Fujimoto, M.; Koyama, H. Resistive switching properties of high crystallinity and low-resistance $Pr_{0.7}Ca_{0.3}MnO_3$ thin film with point-contacted Ag electrodes. *Appl. Phys. Lett.* **2007**, *91*, 223504. [CrossRef]
25. Chang, W.; Liao, J.; Lo, Y.; Wu, T. Resistive switching characteristics in $Pr_{0.7}Ca_{0.3}MnO_3$ thin films on $LaNiO_3$-electrodized Si substrate. *Appl. Phys. Lett.* **2009**, *94*, 172107. [CrossRef]
26. Liao, Z.L.; Wang, Z.Z.; Meng, Y.; Liu, Z.Y.; Gao, P.; Gang, J.L.; Zhao, H.W.; Liang, X.J.; Bai, X.D.; Chen, D.M. Categorization of resistive switching of metal-$Pr_{0.7}Ca_{0.3}MnO_3$-metal devices. *Appl. Phys. Lett.* **2009**, *94*, 253503. [CrossRef]
27. Kim, C.; Chen, I. Effect of top electrode on resistance switching of (Pr, Ca)MnO_3 thin films. *Thin Solid Films* **2006**, *515*, 2726–2729. [CrossRef]
28. Aarik, J.; Aidla, A.; Mändar, H.; Sammelselg, V.; Uustare, T. Texture development in nanocrystalline hafnium dioxide thin films grown by atomic layer deposition. *J. Cryst. Growth* **2000**, *220*, 105–113. [CrossRef]
29. Park, H.B.; Cho, B.B.M.; Park, J.; Lee, S.W.; Hwang, C.S. Comparison of HfO_2 films grown by atomic layer deposition using $HfCl_4$ and H_2O or O_3 as the oxidant. *J. Appl. Phys.* **2003**, *94*, 3641–3647. [CrossRef]
30. Kim, M.-S.; Rodgers, S.; Kim, Y.-S.; Lee, J.-H.; Kang, H.-K. ALD analyses of $HfCl_4$ + O_3 and $HfCl_4$ + H_2O by mass spectroscopy. In *Advanced Gate Stack, Source/Drain and Channel Engineering for Si-based CMOS: New Materials, Processes, and Equipment*; Electrochemical Society, Inc.: Philadelphia, PA, USA, 2005; Volume 5, pp. 397–403. [CrossRef]
31. Delabie, A.; Swerts, J.; van Elshocht, S.; Jung, S.H.; Räisänen, P.I.; Givens, M.E.; Shero, E.J.; Peeters, J.; Machkaoutsan, V.; Maes, J.W. Ozone based atomic layer deposition of hafnium oxide and impact of nitrogen oxide species. *J. Electrochem. Soc.* **2011**, *158*, D259–D263. [CrossRef]
32. Aarik, L.; Arroval, T.; Mändar, H.; Rammula, R.; Aarik, J. Influence of oxygen precursors on atomic layer deposition of HfO_2 and hafnium-titanium oxide films: Comparison of O_3- and H_2O-based processes. *Appl. Surf. Sci.* **2020**, *530*, 147229. [CrossRef]
33. Lo Nigro, R.; Toro, R.G.; Malandrino, G.; Raineri, V.; Fragalà, I.L. A simple route to the synthesis of Pr_2O_3 high-k thin films. *Adv. Mater.* **2003**, *15*, 1071–1075. [CrossRef]
34. Hansen, P.-A.; Fjellvåg, H.; Finstad, T.G.; Nilsen, O. Luminescence properties of lanthanide and ytterbium lanthanide titanate thin films grown by atomic layer deposition. *J. Vac. Sci. Technol. A* **2016**, *34*, 01A130. [CrossRef]
35. Hansen, P.-A.; Fjellvåg, H.; Finstad, T.; Nilsen, O. Structural and optical properties of lanthanide oxides grown by atomic layer deposition (Ln = Pr, Nd, Sm, Eu, Tb, Dy, Ho, Er, Tm, Yb). *Dalton Trans.* **2013**, *42*, 10778–10785. [CrossRef] [PubMed]
36. Aarik, L.; Peetermann, K.; Puust, L.; Mändar, H.; Kikas, A.; Sildos, I.; Aarik, J. Atomic-layer design and properties of Pr-doped HfO_2 thin films. *J. Alloys Compd.* **2021**, *868*, 159100. [CrossRef]
37. Kim, S.K.; Kim, W.-D.; Kim, K.-M.; Hwang, C.S.; Jeong, J. High dielectric constant thin films on a Ru electrode grown at 250 °C by atomic-layer deposition. *Appl. Phys. Lett.* **2004**, *85*, 4112. [CrossRef]
38. Schaekers, M.; Capon, B.; Detavernier, C.; Blasco, N. The deposition of Ru and RuO_2 films for DRAM electrode. *ECS Trans.* **2010**, *33*, 135–144. [CrossRef]
39. Müller, R.; Ghazaryan, L.; Schenk, P.; Wolleb, S.; Beladiya, V.; Otto, F.; Kaiser, N.; Tünnermann, A.; Fritz, T.; Szeghalmi, A. Growth of atomic layer deposited ruthenium and its optical properties at short wavelengths using $Ru(EtCp)_2$ and oxygen. *Coatings* **2018**, *8*, 413. [CrossRef]
40. Vos, M.F.J.; Chopra, S.N.; Verheijen, M.A.; Ekerdt, J.G.; Agarwal, S.; Kessels, W.M.M.; Mackus, A.J.M. Area-selective deposition of ruthenium by combining atomic layer deposition and selective etching. *Chem. Mater.* **2019**, *31*, 3878–3882. [CrossRef]
41. Long, B.; Li, Y.; Jha, R. Switching characteristics of Ru/HfO_2/TiO_{2-x}/Ru RRAM devices for digital and analog nonvolatile memory applications. *IEEE Electron. Dev. Lett.* **2012**, *33*, 706–708. [CrossRef]

42. Feng, Y.; Huang, P.; Zhou, Z.; Ding, X.; Liu, L.; Liu, X.; Kang, J. Negative differential resistance effect in Ru-based RRAM device fabricated by atomic layer deposition. *Nanoscale Res. Lett.* **2019**, *14*, 86. [CrossRef]
43. Koroleva, A.A.; Chernikova, A.G.; Chouprik, A.A.; Gornev, E.S.; Slavich, A.S.; Khakimov, R.R.; Korostylev, E.V.; Hwang, C.S.; Markeev, A.M. Impact of the atomic layer-deposited Ru electrode surface morphology on resistive switching properties of TaO_x-based memory structures. *ACS Appl. Mater. Interfaces* **2020**, *12*, 55331–55341. [CrossRef]
44. Manjunath, V.J.; Rush, A.; Barua, A.; Jha, R. Effect of aluminum interfacial layer in a niobium oxide based resistive RAM. *Solid State Electron. Lett.* **2019**, *1*, 52–57. [CrossRef]
45. Al-Mamun, M.; King, S.W.; Orlowski, M. Thermal and chemical integrity of Ru electrode in $Cu/TaO_x/Ru$ ReRAM memory cell. *ECS J. Solid State Sci. Technol.* **2019**, *8*, N220–N233. [CrossRef]
46. Dueñas, S.; Castán, H.; García, H.; Ossorio, O.G.; Domínguez, L.A.; Seemen, H.; Tamm, A.; Kukli, K.; Aarik, J. The role of defects in the resistive switching behavior of Ta_2O_5-TiO_2-based metal-insulator-metal (MIM) devices for memory applications. *J. Electron. Mater.* **2018**, *47*, 4938–4943. [CrossRef]
47. Waser, R.; Dittmann, R.; Staikov, G.; Szot, K. Redox-based resistive switching memories—Nanoionic mechanisms, prospects, and challenges. *Adv. Mater.* **2009**, *21*, 2632–2663. [CrossRef]
48. Waser, R.; Aono, M. Nanoionics-based resistive switching memories. *Nat. Mater.* **2007**, *6*, 833–840. [CrossRef] [PubMed]
49. Wouters, D.J.; Waser, R.; Wuttig, M. Phase-change and redox-based resistive switching memories. *Proc. IEEE* **2015**, *103*, 1274–1288. [CrossRef]
50. Celano, U. Filamentary-based resistive switching. In *Metrology and Physical Mechanisms in New Generation Ionic Devices*; Theses (Recognizing Outstanding Ph.D. Research); Springer: Berlin/Heidelberg, Germany, 2016.
51. Feng, W.; Shima, H.; Ohmori, K.; Akinaga, H. Investigation of switching mechanism in HfO_x-ReRAM under low power and conventional operation modes. *Sci. Rep.* **2016**, *6*, 39510. [CrossRef]
52. Aldana, S.; García-Fernández, P.; Romero-Zaliz, R.; González, M.B.; Jiménez-Molinos, F.; Gómez-Campos, F.; Campabadal, F.; Roldán, J.B. Resistive switching in HfO_2 based valence change memories, a comprehensive 3D kinetic Monte Carlo approach. *J. Phys. D Appl. Phys.* **2020**, *53*, 225106. [CrossRef]
53. Kim, B.; Mahata, C.; Ryu, H.; Ismail, M.; Yang, B.-D. Kim, S. Alloyed high-k-based resistive switching memory in contact hole structures. *Coatings* **2021**, *11*, 451. [CrossRef]
54. Chen, J.-Y.; Huang, C.-W.; Chiu, C.-H.; Huang, Y.-T.; Wu, W.-W. Switching kinetic of VCM-based memristor: Evolution and positioning of nanofilament. *Adv. Mater.* **2015**, *27*, 5028–5033. [CrossRef] [PubMed]
55. Arroval, T.; Aarik, L.; Rammula, R.; Kruusla, V.; Aarik, J. Effect of substrate-enhanced and inhibited growth on atomic layer deposition and properties of aluminum-titanium oxide films. *Thin Solid Films* **2016**, *600*, 119–125. [CrossRef]
56. Castán, H.; Dueñas, S.; Kukli, K.; Kemell, M.; Ritala, M.; Leskelä, M. Study of the influence of the dielectric composition of $Al/Ti/ZrO_2{:}Al_2O_3/TiN/Si/Al$ structures on the resistive switching behavior for memory applications. *ECS Trans.* **2018**, *85*, 143–148. [CrossRef]
57. Dueñas, S.; Castán, H.; Kukli, K.; Mikkor, M.; Kalam, K.; Arroval, T.; Tamm, A. Memory maps: Reading RRAM devices without power consumption. *ECS Trans.* **2018**, *85*, 201–206. [CrossRef]
58. Fujimori, H.; Yashima, M.; Sasaki, S.; Kakihana, M.; Mori, T.; Tanaka, M.; Yoshimura, M. Cubic-tetragonal phase change of yttria-doped hafnia solid solution: High-resolution X-ray diffraction and Raman scattering. *Chem. Phys. Lett.* **2001**, *346*, 217–223. [CrossRef]
59. Nakajima, R.; Azuma, A.; Yoshida, H.; Shimizu, T.H.; Ito, T.; Shingubara, S. Hf layer thickness dependence of resistive switching characteristics of $Ti/Hf/HfO_2/Au$ resistive random access memory device. *Jpn. J. Appl. Phys.* **2018**, *57*, 06HD06. [CrossRef]
60. Hsieh, C.-C.; Roy, A.; Rai, A.; Chang, Y.-F.; Banerjee, S.K. Characteristics and mechanism study of cerium oxide based random access memories. *Appl. Phys. Lett.* **2015**, *106*, 173108. [CrossRef]
61. Zhao, X.; Vanderbilt, D. First-principles study of structural, vibrational, and lattice dielectric properties of hafnium oxide. *Phys. Rev. B* **2002**, *65*, 233106. [CrossRef]
62. Kato, K.; Sakashita, M.; Takeuchi, W.; Taoka, N.; Nakatsuka, O.; Zaima, S. Importance of control of oxidant partial pressure on structural and electrical properties of Pr-oxide films. *Thin Solid Films* **2014**, *557*, 276–281. [CrossRef]
63. Kondo, H.; Sakurai, S.; Sakashita, M.; Sakai, A.; Ogawa, M.; Zaima, S. Metal-organic chemical vapor deposition of high-dielectric-constant praseodymium oxide films using a cyclopentadienyl precursor. *Appl. Phys. Lett.* **2010**, *96*, 012105. [CrossRef]
64. Liu, F.; Cheng, X.; Mao, J.; Li, S.; Shao, H.; Liu, T.; Yamaguchi, T.; Zeng, X. Fabrication and characterization of Pr_6O_{11}-HfO_2 ultra-high temperature infrared radiation coating. *J. Eur. Ceram. Soc.* **2019**, *39*, 4208–4215. [CrossRef]
65. Ondračka, P.; Holec, D.; Nečas, D.; Zajíčková, I. Accurate prediction of band gaps and optical properties of HfO_2. *J. Phys. D Appl. Phys.* **2016**, *49*, 395301. [CrossRef]
66. He, S.; Hao, A.; Qin, N.; Bao, D. Unipolar resistive switching properties of Pr-doped ZnO thin films. *Ceram. Int.* **2017**, *43*, S474–S480. [CrossRef]
67. McKenna, K.P. Optimal stoichiometry for nucleation and growth of conductive filaments in HfO_x. *Model. Simul. Mater. Sci. Eng.* **2014**, *22*, 025001. [CrossRef]
68. Hong, S.K.; Kim, J.E.; Kim, S.O.; Choi, S.-Y.; Cho, B.J. Flexible resistive switching memory device based on graphene oxide. *IEEE Electron. Dev. Lett.* **2010**, *31*, 1005–1007. [CrossRef]

69. Balatti, S.; Ambrogio, S.; Wang, Z.; Sills, S.; Calderoni, A.; Ramaswamy, N.; Ielmini, D. Voltage-controlled cycling endurance of HfOx-based resistive-switching memory. *IEEE Trans. Electron. Dev.* **2015**, *62*, 3365–3372. [CrossRef]
70. Pérez, E.; Ossorio, Ó.G.; Dueñas, S.; Castán, H.; García, H.; Wenger, C. Programming pulse width assessment for reliable and low-energy endurance performance in Al:HfO_2-based RRAM arrays. *Electronics* **2020**, *9*, 864. [CrossRef]
71. Tan, T.; Guo, T.; Liu, Z. Au doping effects in HfO_2-based resistive switching memory. *J. Alloys Compd.* **2014**, *610*, 388–391. [CrossRef]
72. Ku, B.; Abbas, Y.; Sokolov, A.S.; Choi, C. Interface engineering of ALD HfO_2-based RRAM with Ar plasma treatment for reliable and uniform switching behaviors. *J. Alloys Compd.* **2018**, *735*, 1181–1188. [CrossRef]
73. Ismail, M.; Mahata, C.; Kim, S. Forming-free Pt/Al_2O_3/HfO_2/$HfAlO_x$/TiN memristor with controllable multilevel resistive switching and neuromorphic characteristics for artificial synapse. *J. Alloys Compd.* **2021**, *892*, 162141. [CrossRef]
74. Zrinski, I.; Mardare, C.C.; Jinga, L.I.; Kollender, J.P.; Socol, G.; Minenkov, A.; Hassel, A.W.; Mardare, A.I. Electrolyte-dependent modification of resistive switching in anodic hafnia. *Nanomaterials* **2021**, *11*, 666. [CrossRef] [PubMed]
75. Liu, C.-F.; Tang, X.-G.; Wang, L.-Q.; Tang, H.; Jiang, Y.-P.; Liu, Q.-X.; Li, W.-H.; Tang, Z.-H. Resistive switching characteristics of HfO_2 thin films on mica substrates prepared by sol-gel process. *Nanomaterials* **2019**, *19*, 1124. [CrossRef] [PubMed]
76. Sun, C.; Lu, S.M.; Jin, F.; Mo, W.Q.; Song, J.L.; Dong, K.F. Control the switching mode of Pt/HfO_2/TiN RRAM devices by tuning the crystalline state of TiN electrode. *J. Alloys Compd.* **2018**, *749*, 481–486. [CrossRef]